



Single-atomic ruthenium coupling with NiFe layered double hydroxide in-situ growth on BiVO₄ photoanode for boosting photoelectrochemical water splitting

Yunshuyu Sun^a, Hao Li^a, Yao Hu^a, Jinnan Wang^{a,*}, Aimin Li^a, Philippe François-Xavier Corvini^b

^a State Key Laboratory of Pollution Control and Resource Reuse & School of the Environment Nanjing University, Nanjing 210023, China

^b School of Life Sciences, University of Applied Sciences and Arts Northwestern Switzerland, Basel 4132, Switzerland

ARTICLE INFO

Keywords:

Single-atomic Ru
NiFe Layered Double Hydroxide
BiVO₄ photoanode
Photoelectrochemical water splitting
Oxygen evolution reaction

ABSTRACT

In the present work, NiFe layered double hydroxide (LDH) supported single Ru atoms in-situ growth on BiVO₄ photoanode (BiVO₄@NiFe-LDHs/Ru) was fabricated to enhance the photoelectrochemical (PEC) water splitting. Ru atoms anchored to NiFe-LDHs via oxygen coordination to form Ru-O-M bonds, which induced electrons rearrangement to improve charge carriers separation and injection. Combining with the synergistic effect of Ru and NiFe-LDHs, BiVO₄@NiFe-LDHs/Ru achieves high photocurrent density of 4.65 mA/cm² at 1.23 V vs. RHE. Besides, Ru atoms induced formation of V^{(5-x)+} to stabilize V atoms in the lattice of BiVO₄, which avoided V⁵⁺ dissolution during PEC water oxidation process. Density functional theory (DFT) calculation indicates that Ru SAs anchored to BiVO₄@NiFe-LDHs decrease the reaction energy barrier of rate-limiting step (*O → *OOH), resulting in acceleration of OER process. This work provides an effective pathway to design high efficient and stable photoanodes with single atoms for feasible PEC water splitting application.

1. Introduction

With the increase of demand for clean energy, PEC water splitting has arisen great interest in solar energy utilization since 1972 [1–5]. Generally, PEC water splitting process included hydrogen evolution reactions (HER) and oxygen evolution reactions (OER). Most cases demonstrated that OER is the rate determining step of the water splitting due to its four-electron nature and sluggish kinetics [6,7]. Therefore, development of efficient photoanode is the key challenge for construction of PEC system.

For improvement of OER, much attention was focused on the exploration of photoanode with high light harvesting, superior conductivity and photocarriers separation [8–12]. Owing to high theoretical solar-to-hydrogen conversion efficiency (9.2 %) and photocurrent (7.5 mA/cm² under standard AM 1.5 G solar light), suitable band gap (~2.4 eV) and adequate positive valence band edge (VB, ~2.4 eV), bismuth vanadate (BiVO₄) was considered as the one of the most promising photocatalyst for water oxidation and organics degradations [13]. However, the practical photocatalytic efficiency of BiVO₄ is much

lower than what is expected due to serious carriers recombination and low visible-light utilization [14]. Thus, it is expected to improve the catalytic activity of BiVO₄ by introduction of co-catalysts.

Although noble metal Ir and Ru containing compounds including RuO₂ and IrO₂ exhibit considerable OER performance in the basic electrolyte [15–19], their wide-scale application is severely hindered due to hefty costs and instability. It was reported that RuO₂ catalysts are unstable under high anodic potentials and tend to dissolve into electrolyte because of conversion to high oxidation states [20,21]. On the other hand, single-atom catalysts (SACs) with smaller dimensions and higher surface-to-volume ratios are currently developed, which could not only lower catalyst cost but also exploiting catalytic performance through size effect [22]. Thus, introduction of SACs into photo-anode might improve the OER performance by adjusting charge distribution and coordination environment [23,24]. However, pushing catalysts to single atom scale is nontrivial because SACs with thermodynamical instability tend to aggregate into clusters or nanoparticles [25]. Thus, it is necessary to stabilize the single atoms with a support, such as carbon materials, metals, metal oxide, metal-organic frameworks, and boron

* Corresponding author.

E-mail address: wjnnju@163.com (J. Wang).

<https://doi.org/10.1016/j.apcatb.2023.123269>

Received 15 July 2023; Received in revised form 28 August 2023; Accepted 4 September 2023

Available online 6 September 2023

0926-3373/© 2023 Elsevier B.V. All rights reserved.

nitride [26–30].

As a widely used two-dimensional cocatalyst, layered double hydroxides (LDHs) have attracted intense attention due to their low overpotential and high OER activity under alkaline conditions [31–34]. Transition metals including Ni and Fe were introduced into LDHs for enhancement of OER performance due to the formation of Ni-Fe oxyhydroxide in situ on the surface of NiFe-LDHs, which can not only reduce Fe–O bond length in $\gamma\text{-Ni}_{1-x}\text{Fe}_x\text{OOH}$ compared with in $\gamma\text{-FeOOH}$ but also modify the crystal structure for facilitating adsorption energies of OER intermediates optimization [35,36]. Previous work also demonstrated that NiFe-LDH loaded onto BiVO_4 as cocatalysts could construct heterojunctions for enhancing light absorption and transition metal active sites utilization [34]. On the other hand, although large amounts of alkali-active site on LDHs surface can provide special anchoring sites for SACs, poor charge carrier transfer and inadequate active edge sites of LDHs still remain to be improved [37]. Previous work demonstrated that construction of charge carriers transfer channel between LDHs and noble metals could significantly accelerate the charge carriers transfer [38,39].

Herein, $\text{BiVO}_4/\text{NiFe-LDHs}$ anchored with the ruthenium single atoms ($\text{BiVO}_4/\text{NiFe-LDHs}/\text{Ru}$) was constructed for enhancement of OER performance. Fourier transform-extended X-ray absorption fine structure (XAFS) spectra and spherical aberration-corrected scanning transmission electron microscope (Cs-corrected STEM) images clearly show Ru atoms well anchored to NiFe-LDHs through oxygen coordination bonds and keep atomic isolated. XPS and EIS analyses demonstrate that Ru SAs anchored to $\text{BiVO}_4/\text{NiFe-LDHs}$ not only change the electron cloud density but also decrease the resistance of the photoanode. Notably, DFT calculations suggest that Ru–O–M (M = Ni or Fe) bonds formed between Ru SAs and transition metals induced the spatial electron rearrangement and decrease the reaction energy barrier of rate-limiting step ($\text{*O} + \text{OH}^- \rightarrow \text{*OOH} + \text{e}^-$). Subsequently, $\text{BiVO}_4/\text{NiFe-LDHs}/\text{Ru}$ achieves high photocurrent density of $4.65 \text{ mA}/\text{cm}^2$ at 1.23 V vs.RHE at AM 1.5 G (100 mW cm^{-2}), and it can remain 94.8 % of the value of initial photocurrent density within 5 h. In summary, the present work not only provided new ideas to decrease reaction energy barrier of rate-determining step of OER, but also expanded the application of Ru SAs in PEC water splitting.

2. Experimental section

2.1. Materials

Bismuth nitrate pentahydrate [$\text{Bi}(\text{NO}_3)_3 \cdot 5\text{H}_2\text{O}$, 99.0 %], the hydrochloric acid (HCl, GR), nitric acid (HNO_3 , GR), sodium nitrate (NaNO_3 , 99.0 %) and sodium hydroxide (NaOH, 96.0 %) were purchased from Aladdin, anhydrous sodium sulfate (Na_2SO_4 , 99.5 %) and sodium sulfite (Na_2SO_3 , 98.0 %) were purchased from Nanjing Chemical Reagent Co., Ltd, and dimethyl sulfoxide ($\text{C}_2\text{H}_6\text{SO}$, 99.8 %). Ferrous sulfate heptahydrate ($\text{FeSO}_4 \cdot 7\text{H}_2\text{O}$, 99 %), nickel sulfate hexahydrate ($\text{NiSO}_4 \cdot 6\text{H}_2\text{O}$, 99.9 %), vanadium oxyacetonate ($\text{C}_{10}\text{H}_{14}\text{O}_5\text{V}$, 99.0 %), Ruthenium trichloride hydrate ($\text{RuCl}_3 \cdot x\text{H}_2\text{O}$, 98 %) were purchased from Shanghai Macklin Biochemical Co., Ltd. All the chemicals were used directly in the experiment without any further purification.

2.2. Preparation of $\text{BiVO}_4/\text{NiFe-LDHs}/\text{Ru}$ photoanodes

2.2.1. Preparation of BiVO_4 photoanodes

The BiVO_4 nanofilms were synthesized according to the method reported in previous literatures [40]. 0.970 g of $\text{Bi}(\text{NO}_3)_3 \cdot 5\text{H}_2\text{O}$ was added in 50.0 mL of KI solution (0.4 M) with the adjustment of pH to 1.7 using HNO_3 , and then 20.0 mL p-benzoquinone ethanol solution (0.23 M) was added in the solution. The electrodeposition of BiOI film on FTO ($1 \times 1.5 \text{ cm}^2$, active area $1 \times 1 \text{ cm}^2$) was conducted using typical three-electrode cell with a FTO glass substrate working electrode, Pt wire counter electrode and saturated Ag/AgCl reference electrode.

The deposition procedure was performed at -0.1 V versus Ag/AgCl for 200 s to obtained BiOI electrodes. After rinsed with deionized water and dried at 25°C for 1 h, 150 μL of a dimethyl sulfoxide solution containing 0.2 M vanadyl acetylacetonate [$\text{VO}(\text{acac})_2$] was dropwise added onto the BiOI electrodes. For conversion of BiOI to BiVO_4 , the electrodes samples were heated in muffle furnace at 450°C for 2 h with the ramping rate of $2^\circ\text{C}/\text{min}$. Then, BiVO_4 electrodes were soaked in 1.0 M NaOH solution for 1 h for removal of residual V_2O_5 , and the obtained yellow electrodes were denoted as bare BiVO_4 .

2.2.2. Preparation of $\text{BiVO}_4/\text{NiFe-LDHs}$ photoanodes

50 mL of KBi solution (0.5 M) was aerated with argon for 10 min to remove the oxygen. Then 43.4 mg of $\text{NiSO}_4 \cdot 6\text{H}_2\text{O}$ and 20 mg of $\text{FeSO}_4 \cdot 7\text{H}_2\text{O}$ were added into KBi solution with stirring for 10 min in argon atmosphere. The electrodeposition process was performed by using a three-electrode system with the constant current at 0.02 mA for 480 s, in which platinum electrode, Ag/AgCl electrode and BiVO_4 photoanode acted as the counterelectrode, reference electrode and working electrode respectively. The obtained $\text{BiVO}_4/\text{NiFe-LDHs}$ electrode was washed with deionized water and dried for further research.

2.2.3. Preparation of $\text{BiVO}_4/\text{NiFe-LDHs}/\text{Ru}$ photoanodes

50 μL of RuCl_3 methanol solution (1 g/L) was dropped into 10 mL mixture of methanol and ammonia ($V_{\text{methanol}}/V_{\text{ammonia}} = 3:1$) with ultrasonic. Then, the suspension was transferred into a 25.0 mL autoclave with the fabricated $\text{BiVO}_4/\text{NiFe-LDHs}$ electrodes facing downward. After ultrasonic for 30 min at 100 W power, the autoclave was heated at 60°C for 10 h. The obtained $\text{BiVO}_4/\text{NiFe-LDHs}/\text{Ru}$ photoanode was cleaned with deionized water and ethanol for several times, then dried for subsequent use.

2.3. Photoelectrochemical measurements

PEC measurements were performed on an electrochemical workstation (CHI760E, CH Instruments, Inc.). Ag/AgCl (saturated KCl) and platinum sheet were used as reference electrode and counter electrode in a three-electrode battery system, respectively. A 300 W Xe lamp (PLS-SXE300D) was used as the light source on the back of the sample, and all samples were measured under backlit conditions with an illuminated area of 1 cm^2 (AM 1.5 G, 100 mW cm^{-2}). 0.5 M potassium borate (pH = 9.33) was used as the electrolyte. Both charge separation and injection efficiency were determined by using 0.2 M Na_2SO_3 as a hole scavenger oxidation measure. According to Nernst equation Eq. (1), potential vs. RHE can be calculated from the potential vs. Ag/AgCl.

$$E_{\text{RHE}} = E_{\text{Ag/AgCl}} + 0.0591 \times \text{pH} + E_{\text{Ag/AgCl}}^0 \quad (1)$$

E_{RHE} represents the converted potential versus RHE, while $E_{\text{Ag/AgCl}}$ refers to the obtained potential versus Ag/AgCl electrode. The normal potential of Ag/AgCl electrode ($E_{\text{Ag/AgCl}}^0$) is 0.1976 V at 25°C . Both surface charge injection efficiency (η_{inj}) and charge separation efficiency (η_{sep}) can be calculated according to Eqs. (2–3).

$$\eta_{\text{inj}} (\%) = \frac{J_{\text{water}}}{J_{\text{Na}_2\text{SO}_3}} \quad (2)$$

$$\eta_{\text{sep}} (\%) = \frac{J_{\text{Na}_2\text{SO}_3}}{J_{\text{abs}}} \quad (3)$$

where J_{water} and $J_{\text{Na}_2\text{SO}_3}$ are photocurrent densities of the water oxidation and sulfite oxidation, respectively. J_{abs} represents the theoretical photocurrent density, which is based on the assumption of that the photons absorbed are completely converted to the current. In addition, applied bias photon to current efficiency (ABPE) can be calculated according to the LSV curves by Eq. (4):

$$ABPE(\%) = \frac{J \times (1.23 - V_{bias})}{P_{AM1.5}} \times 100\% \quad (4)$$

where J is the photocurrent density (mA cm^{-2}) indicated by LSV curves. V_{bias} represents the applied bias versus RHE (V), and $P_{AM1.5}$ is 100 mW cm^{-2} . The incident photon-to-current conversion efficiency (IPCE) is calculated based on the determination of photocurrent densities at specific wavelengths using the light source with a monochromator (Eq. 5):

$$IPCE(\%) = \frac{1240 \times J}{\lambda \times P_{light}} \times 100\% \quad (5)$$

Where P_{light} and J represent the light power density and photocurrent density at a specific wavelength, respectively. And λ refers to incident wavelength. In addition, within the frequency ranges of 0.1–100000 Hz, both photoelectrochemical impedance spectroscopy (PEIS) under AM 1.5 G illumination and electrochemical impedance spectroscopy (EIS) in dark condition were conducted with an AC voltage amplitude of 5 mV at the open-circuit potential. Mott-Schottky (MS) measurements were performed at different frequencies (1000 Hz and 500 Hz) using potassium borate (0.5 M, pH = 9.33) as the electrolyte solution. According to Eq. (6), the charge carrier densities (N_d) can be calculated based on the MS curves measured at 1000 Hz in the dark.

$$N_d = \left(\frac{2}{e\epsilon\epsilon_0} \right) \left[\frac{d(1/C^2)}{dV} \right]^{-1} \quad (6)$$

Herein, the electron charge e , the vacuum permittivity ϵ_0 , and the relative permittivity of BiVO_4 are $1.6 \times 10^{-19} \text{ C}$, $8.85 \times 10^{-14} \text{ F cm}^{-1}$ and 68, respectively. The V is the applied bias for MS plots.

To evaluate the H_2 and O_2 production and Faradaic efficiency, after purifying the KBI electrolyte (0.5 M, pH = 9.33) by nitrogen for 30 min, the photocurrent densities of the film are measured at 1.23 V vs. RHE under AM 1.5 G illumination for 3 h, and the production of H_2 and O_2 was detected with a gas chromatograph (9790 II, Fuli, Zhejiang) every 20 min. Meanwhile, the theoretical volume of gas production is calculated by integrating the recorded J -t curves. The ratio of the actual gas volume to the theoretical gas volume is the Faraday efficiency.

2.4. Characterization

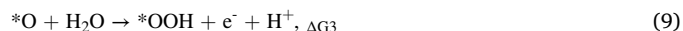
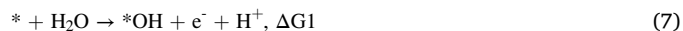
SEM images were conducted by a Zeiss Gemini 300 scanning electron microscope. Transmission electron microscopy (TEM) and high-resolution transmission electron microscopy (HRTEM) were performed (FEI TF20). Crystal structures were identified by X-ray diffraction analysis (XRD) with $\text{Cu K}\alpha$ radiation (1.5406 \AA) in the 2θ range of $5\text{--}80^\circ$ using an XRD-6000 X-ray diffractometer (Shimadzu, Japan). X-ray photoelectron spectroscopy (XPS) was analyzed using monochromatic $\text{Al K}\alpha$ radiation by the PHI 5000 Versa Journal Prevalidation probe instrument. The C1s peak at 284.8 eV was used as reference for all binding energies. The optical property of the electrode was determined by UV–vis absorption spectrum using a UV-2600 spectrophotometer (Shimadzu, Japan). Photoluminescence spectra (PL) were measured at room temperature with a 405 nm excited laser in Fluoromax-4 fluorescence spectrophotometer. The single atom image was collected on a FEI Themis Z spherical aberration-corrected scanning transmission electron microscope (Cs-corrected STEM). ICP-MS was performed with a Thermo-Fisher icap7400 on nitric acid dissolution in BiVO_4 @NiFe-LDHs/Ru sample. Ru K-edge analysis was performed with Si (111) crystal monochromators at the BL11B beamlines at the Shanghai Synchrotron Radiation Facility (SSRF) (Shanghai, China). Before the analysis at the beamline, samples were pressed into thin sheets with 1 cm in diameter and sealed using Kapton tape film. The XAFS spectra were recorded at room temperature using a 4-channel Silicon Drift Detector (SDD) Bruker 5040. Ru K-edge extended X-ray absorption fine structure (EXAFS) spectra were recorded in transmission mode. The XAFS spectra

of these standard samples (Ru foil, RuCl_3 , RuO_2) were recorded in transmission mode. The spectra were processed and analyzed by the software codes Athena and Artemis.

2.5. Computational details

All computations were performed by density functional theory (DFT) method in Vienna ab initio simulation package (VASP) [41,42]. On the basis of BiVO_4 , slice (001) surface, expose Bi and V metal elements at the terminal, determine the growth mechanism of LDHs, construct the NiFe-LDHs and BiVO_4 heterogeneous junction model. The generalized gradient approximation in the Perdew-Burke-Ernzerhof functional (GGA-PBE) was used to treat the electron exchange and correlation energy [43]. The valence orbitals of V (3p, 3d, 4 s), Bi (6 s, 6p), Fe (3p, 3d, 4 s), Ni (3p, 3d, 4 s), Ru (4p, 4d, 5 s), C (2 s, 2p), O (2 s, 2p) and H (1 s) were described by plane-wave basis sets with cutoff energies of 500 eV. According to the Materials Project online database, the Ueff value of Fe, Ni and V is 2.5 eV. The k-point sampling was set using the Monkhorst-Pack scheme with a $(3 \times 3 \times 1)$ mesh for the surface models with and without adsorbates, and a $(1 \times 1 \times 1)$ mesh for single-molecule adsorbates. The convergence criteria for the electronic self-consistent iteration and force were set to 10^{-5} eV and 0.02 eV \AA^{-1} , respectively.

The four-electron pathway of OER occurs in alkaline aqueous solution was generally reported to proceed according to the following steps [44].

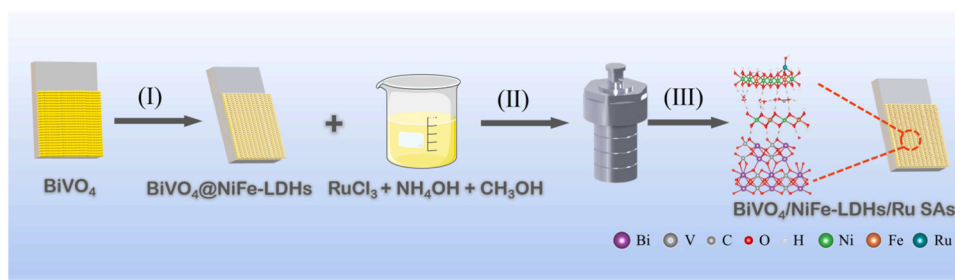


Where “*” represents the active site on the catalyst, and $*O$, $*OH$, and $*OOH$ are the intermediates of adsorption. By Eq.11, the Gibbs free energy of OER process can be calculated based on adsorption energy of intermediate products (E_{abs}), zero point energy of reaction (ΔE_{ZPE}) and entropy (ΔS). Herein, ΔU is the energy difference between 0 K and temperature t . Overpotential is defined as $\eta = \max[34 \Delta G_4] / e - 1.23 \text{ V}$. [$\Delta G = E_{abs} + \Delta E_{ZPE} - T\Delta S + \Delta U(0 \rightarrow T)$],

3. Results and discussion

3.1. Characterization of photoanodes

Due to the similar ionic radii of Fe^{3+} (64.5 pm), Ni^{2+} (69 pm), and Ru^{3+} (68 pm) (Table S1), Ru SAs are anchored to NiFe-LDHs after hydrothermal action (Scheme 1). SEM images showed that BiVO_4 @NiFe-LDHs/Ru nanorods with wormlike shape and smooth surface are uniformly loaded onto the FTO as well as bare BiVO_4 and BiVO_4 @NiFe-LDHs (Fig. 1a, S1), which is beneficial to molecular diffusion and light absorption [45]. In addition, BiVO_4 with the lattice width of 0.309 nm can be found from HR-TEM images which shows the completely exposed of {121} crystal facet, and provides a growth interface for NiFe-LDHs [46]. An ultrathin layer (3–5 nm) of NiFe-LDHs outside the BiVO_4 can be clearly observed (Fig. 1b, c), which not only facilitates the uniform dispersion of Ru SAs on BiVO_4 @NiFe-LDHs/Ru but also reduces the optical loss as incident light pass through the NiFe-LDHs. As cocatalyst which connect BiVO_4 via $-\text{O}-\text{H}-\text{O}-$ bond (Fig. S5), two-dimensional structure of LDHs can shorten the diffusion distance of holes, which also promoted holes migration from BiVO_4 to photoanode surface so as to inhibit recombination of photogenerated carriers. Notably, Cs-corrected STEM images (Fig. 1d, e, S2) clearly show that Ru SAs are uniformly dispersed on the surface of LDHs, without cluster or aggregation. By using ICP-MS, the content of Ru in BiVO_4 @NiFe-LDHs/Ru



Scheme 1. (I) $\text{BiVO}_4\text{@NiFe-LDHs}$ was prepared by electrodeposition of Fe^{2+} and Ni^{3+} in KBI solution. (II) Transfer the electrode to the reactor and fix it, and ultrasonic with the prepared NH_4OH solution of Ru^{3+} for 30 min (III) $\text{BiVO}_4\text{@NiFe-LDHs/Ru}$ photoanodes were prepared by heating the reactor at 60°C for 600 min.

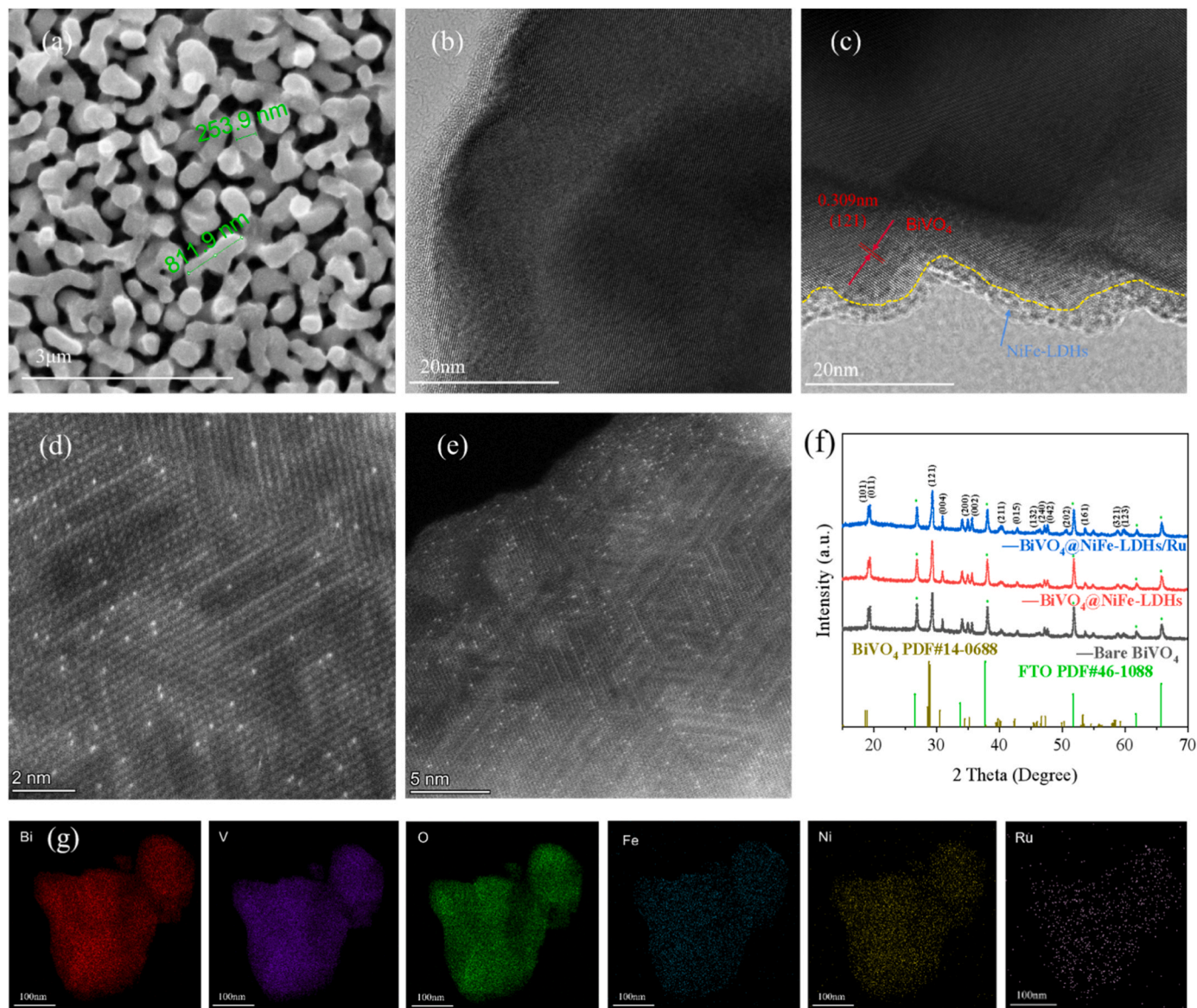


Fig. 1. (a) SEM image, (b) TEM image, (c) HRTEM image, (d, e) Cs-corrected STEM images of $\text{BiVO}_4\text{@NiFe-LDHs/Ru}$ photoanode. (f) XRD patterns of BiVO_4 , $\text{BiVO}_4\text{@NiFe-LDHs}$ and $\text{BiVO}_4\text{@NiFe-LDHs/Ru}$. (g) Energy-dispersive X-ray spectroscopy (EDS) mapping of $\text{BiVO}_4\text{@NiFe-LDHs/Ru}$, scale bar: 100 nm.

was determined as 0.34 % (Table S2), which is within the normal range as previous literature reported [24]. Furthermore, other metals contents are also determined, which followed the order of $\text{Bi} > \text{V} > \text{Fe} > \text{Ni}$. EDS analysis (Fig. 1g) directly confirms the uniform dispersion of these elements on $\text{BiVO}_4\text{@NiFe-LDHs/Ru}$ photoanode, and the surface elements

contents also follow the order above. Interestingly, characteristic peaks of Ru, Ni/Fe are not observed in XRD spectra (Fig. 1f), which can be explained as follows: (1) trace content of Ru anchored to LDH are single atoms, which can not form new crystalline faces; (2) amorphous state of NiFe-LDHs layer can not be observed in XRD spectra [47].

Additionally, X-ray absorption near-edge structure (XANES) was conducted to analyze the coordination structure and oxidation state of Ru SAs in $\text{BiVO}_4/\text{NiFe-LDHs}/\text{Ru}$. XANES spectra (Fig. 2a) is processed by using first derivative, and applying their maximum to determine the Ru K-edge position of $\text{BiVO}_4/\text{NiFe-LDHs}/\text{Ru}$. Generally, there is an approximately linear relationship between absorption edge energy and the calculated oxidation state. The position of the Ru K-edge in $\text{BiVO}_4/\text{NiFe-LDHs}/\text{Ru}$ (22,115.9 eV) located between Ru foil (22,106.1 eV) and RuCl_3 (22,117.0 eV) (Fig. S6), suggests a special oxidation state of Ru SAs ($0 \sim +3$). By fitting the Ru oxidation state as a function of Ru K-edge energy shift (Fig. S7), the average valence state of Ru can be calculated that is $\approx +2.2$. Furthermore, the local structures of coordination nearby Ru atoms are analyzed by using Fourier transform extended X-ray absorption fine structure (EXAFS) spectra (Fig. 2b) together with its corresponding fittings (Fig. 2c). Different from reference samples (Ru foil, RuO_2 , and RuCl_3), $\text{BiVO}_4/\text{NiFe-LDHs}/\text{Ru}$ sample has strong bond of Ru-O at 1.62 Å in the first shell and weak bond of Ru-O-M ($M = \text{Ni}$ or Fe) in the higher energy level. Ru-Ru bond (2.41 Å), Ru-O-Ru bond (3.17 Å), and Ru-Cl bond (1.83 Å) are not observed, suggesting the absent of RuCl_3 [48]. Besides, model-based EXAFS fitting (Table S3) further demonstrates that each Ru atom is coordinated with 4.4 ± 0.5 oxygen atoms where 3.3 ± 0.2 Ru-O are bonded with Ni or Fe. Thus, it can be concluded that Ru atoms are located on the surface of the NiFe-LDHs with isolated single atomic structure instead of agglomeration in the LDHs layers. Notably, different from reference samples, a strong peak of Ru-O coordination in the wavelet transforms (WT) of Ru K-edge EXAFS oscillations (Fig. 2d), can directly confirm the existence of Ru SAs on NiFe-LDHs supporter.

XPS can provide useful information of chemical composition and changes of $\text{BiVO}_4/\text{NiFe-LDHs}$ and $\text{BiVO}_4/\text{NiFe-LDHs}/\text{Ru}$. Obvious positive shifts of binding energies (V, Bi and O) are observed after loading of NiFe-LDHs (Fig. S11), suggesting the strong interaction

between NiFe-LDHs and BiVO_4 . The redox between $\text{Ni}^{2+}/\text{Fe}^{2+}$ and $\text{Ni}^{3+}/\text{Fe}^{3+}$ can accelerated the water oxidation kinetics [34]. More importantly, Ru SAs with strong electronegativity introduced into $\text{BiVO}_4/\text{NiFe-LDHs}$ changes the electron cloud density, thus both positive shifts and negative shifts of binding energy peaks [Bi 4f7/2 (+0.45 eV); V 2p (+0.37 eV); Fe 2p3/2 (−0.15 eV); Ni 2p3/2 (−0.23 eV)] are observed (Fig. 3a-d), indicating that the electron coupling between Ru SAs and NiFe-LDHs occurs [49]. The increased electron cloud density of Ni/Fe proves the electron transfer from Ru to Ni and Fe via the Ru-O-M bond, which facilitate the transfer of holes from BiVO_4 to NiFe-LDHs for OER [10,50], while decreased electron cloud density of V/Bi contribute to the accumulation of photogenerated electrons for HER. Notable, new characteristic peak of Ru-O is observed after Ru SAs was introduced into $\text{BiVO}_4/\text{NiFe-LDHs}$ (Fig. 3e). Herein, the binding energy of Ru 3p3/2 in $\text{BiVO}_4/\text{NiFe-LDHs}/\text{Ru}$ (Fig. 3f) indicates the special valence state between (0) and (+3), which matches the results obtained by EXAFS, and the relatively low valence state is beneficial to inhibit the dissolution of Ru elements since Ru with high valence are unstable under high anodic potentials. In addition, a new shoulder peak representing of low-valent V ($^{5-x}+$) (Fig. 6b) is observed at 515.8 eV and existed even after 5 h reaction, which suggests that Ru atoms induced formation of $\text{V}^{(5-x)+}$ to stabilize V atoms in the lattice of BiVO_4 , avoiding the V^{5+} dissolution during the PEC water oxidation process [51].

3.2. Photoelectrochemical (PEC) water splitting performance

Due to the synergistic effect of monatomic Ru and NiFe-LDHs, $\text{BiVO}_4/\text{NiFe-LDHs}/\text{Ru}$ ($4.65 \text{ mA}/\text{cm}^2$ at 1.23 V vs. RHE) achieves much higher photocurrent density than BiVO_4 ($1.70 \text{ mA}/\text{cm}^2$) and $\text{BiVO}_4/\text{NiFe-LDHs}$ ($3.59 \text{ mA}/\text{cm}^2$) (Fig. 4a), which also performed better than most reported BiVO_4 -based photoanodes (Table S4). In addition, as the proof of effective interfacial charge transfer and

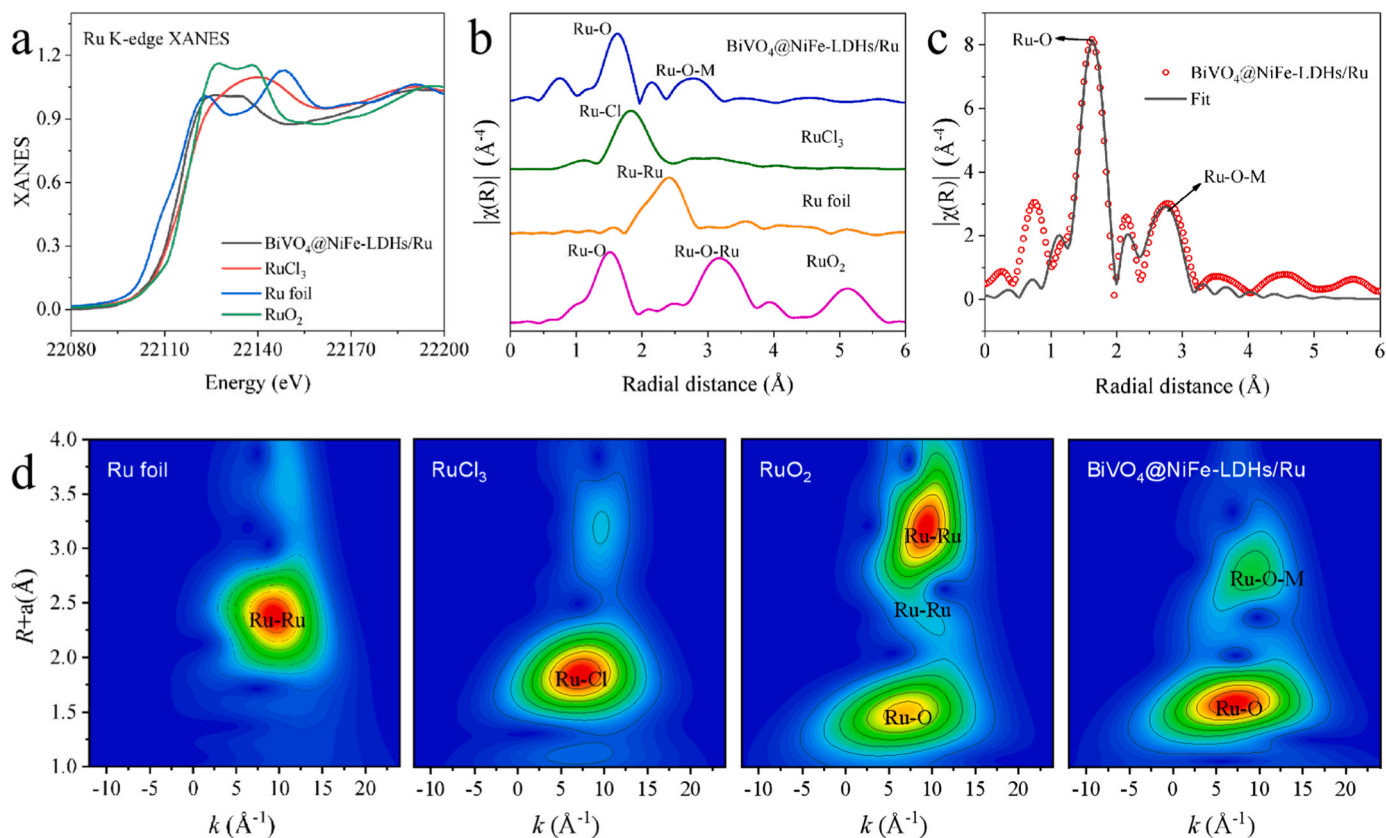


Fig. 2. (a) XANES spectra, (b) R-space Ru K-edge EXAFS spectra, (c) EXAFS R-space fitting curve and (d) WT-EXAFS signals of Ru foil, RuCl_3 , RuO_2 and $\text{BiVO}_4/\text{NiFe-LDHs}/\text{Ru}$.

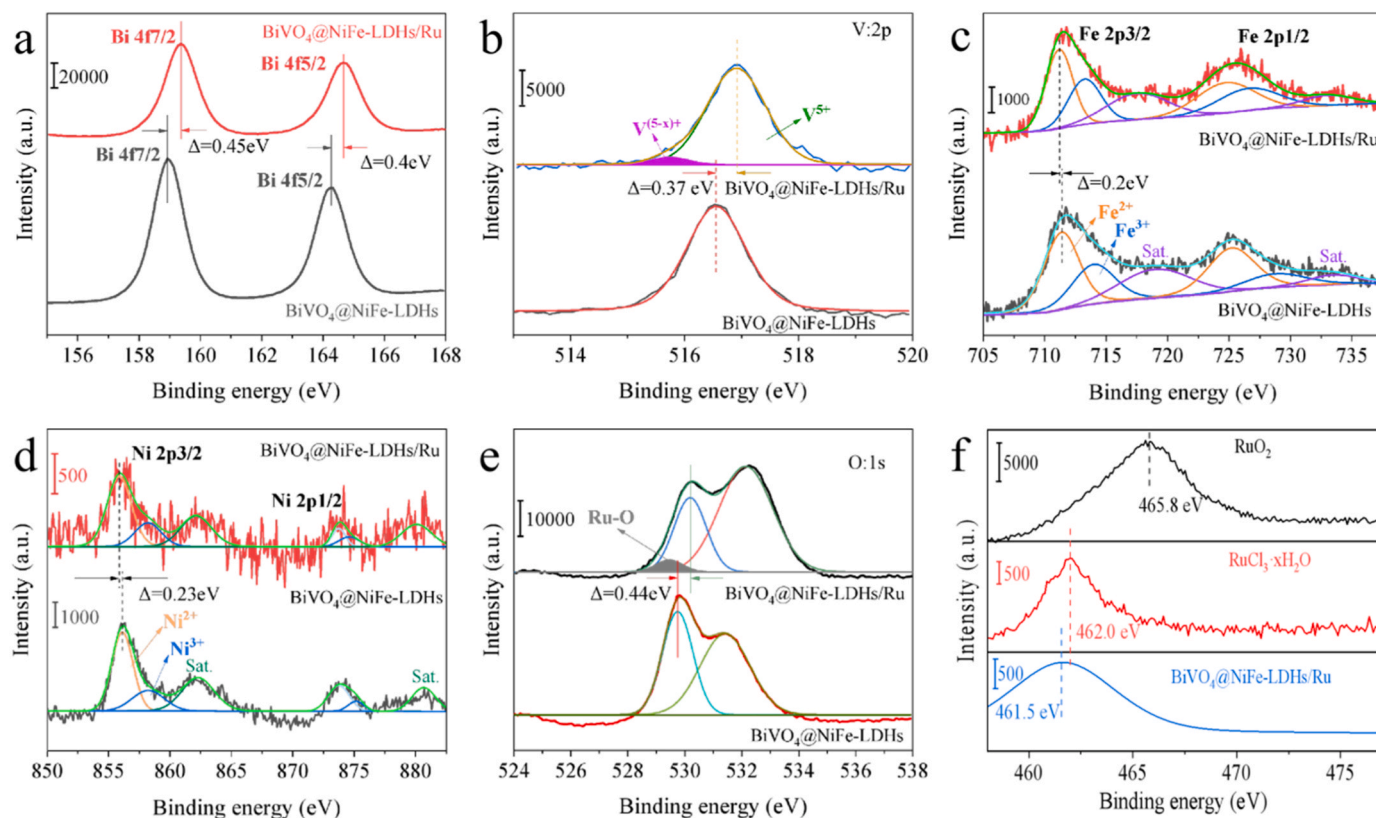


Fig. 3. XPS spectra of $\text{BiVO}_4/\text{NiFe-LDHs}$ and $\text{BiVO}_4/\text{NiFe-LDHs/Ru}$ photoanodes: (a) Bi 4f, (b) V 2p, (c) Fe 2p, (d) Ni 2p, (e) O 1s, (f) Ru in $\text{RuCl}_3 \cdot x\text{H}_2\text{O}$, RuO_2 and $\text{BiVO}_4/\text{NiFe-LDHs/Ru}$.

inhibition of surface-charge recombination caused by Ru SAs, the onset potential of $\text{BiVO}_4/\text{NiFe-LDHs/Ru}$ (0.29 V vs.RHE) (Fig. 4b) decline by 50 mV compared with $\text{BiVO}_4/\text{NiFe-LDHs}$, indicates that the separated dispersed Ru SAs contribute significantly to the acceleration of OER dynamics. As shown in (Fig. S12), the phototransient response of the material was tested. When the light was turned on, the transient peak was basically eliminated because the cocatalyst layer could reduce the charge recombination at the interface. All photoanodes have a light response in the chopper light cycle, and the current is close to zero in the absence of light. Therefore, it is reasonable to infer that the splitting of water is driven by photogenic charge carriers. Besides, the incident photon-to-current conversion efficiency (IPCE) of $\text{BiVO}_4/\text{NiFe-LDHs/Ru}$ is remarkably enhanced in overall optical response range (340–550 nm) (Fig. 4c). In addition, the applied bias photon current efficiency (ABPE) can be measured on the basis of LSV results (Fig. 4d). The maximum ABPE of $\text{BiVO}_4/\text{NiFe-LDHs/Ru}$ is found to be 1.40 % at a relatively low bias of 0.73 V vs.RHE. Greater than that of $\text{BiVO}_4/\text{NiFe-LDHs}$ (0.88 % at 0.81 V vs.RHE) and 4.67 times greater than the bare BiVO_4 (0.30 % at 0.89 V vs.RHE).

Moreover, neither light absorption wavelength (300–500 nm) nor band gap (2.536 eV) were changed after introduction of NiFe-LDHs/Ru into BiVO_4 according to UV–vis spectra and Tauc diagram (Fig. S13, 14), which suggest the enhancement of the photocurrent was not attributed to the improvement of light collection. In order to compare the bulk charge separation efficiency η_{sep} and charge injection efficiency η_{inj} , 0.2 M Na_2SO_3 was added to 0.5 M KBI electrolyte as a hole scavenger (Fig. S15), the η_{inj} (Fig. 4e) of three samples follows the order of $\text{BiVO}_4/\text{NiFe-LDHs/Ru}$ (81.4 %) > $\text{BiVO}_4/\text{NiFe-LDHs}$ (71.5 %) > BiVO_4 (40 %), indicating that $\text{BiVO}_4/\text{NiFe-LDHs/Ru}$ photoanode can provide much more holes for water oxidation [52]. Besides, the highest η_{sep} (86.67 %) of $\text{BiVO}_4/\text{NiFe-LDHs/Ru}$ among three samples (Fig. 4f) demonstrates that the recombination of charge carriers in the bulk phase

of composition was well inhibited. In addition, the weakest PL peak of $\text{BiVO}_4/\text{NiFe-LDHs/Ru}$ suggests the weakest carrier recombination (Fig. 4g). Transient photovoltage (TPV) measurements are conducted to further investigate the lifetimes of photogenerated holes (Fig. S16) [53]. The probability-weighted average decay time (τ_{ave}) of TPV decay curves, which represents the average charge recombination kinetics of photoanodes [54], can be calculated based on the time constants (τ_1 and τ_2) and probability constants (ϕ_1 and ϕ_2) (Fig. S16). τ_{ave} of $\text{BiVO}_4/\text{NiFe-LDHs/Ru}$ is about 62.89 μs , which is 2.58 times higher than that of $\text{BiVO}_4/\text{NiFe-LDHs}$ (24.37 μs) (Table S5). Herein, both PEIS and EIS measurements are conducted. The semicircles for three samples are almost the same under dark condition (EIS) (Fig. S17), while the semicircle of $\text{BiVO}_4/\text{NiFe-LDHs/Ru}$ was much smaller than that for other two electrodes under illuminated conditions (Fig. 4h). Charge carriers recombination of $\text{BiVO}_4/\text{NiFe-LDHs/Ru}$ was inhibited efficiently, which significantly improve the conductivity of $\text{BiVO}_4/\text{NiFe-LDHs/Ru}$. By using ZsimDemo software, PEIS results are fit by the equivalent circuit model inset. Herein, R_s represents the resistance of FTO glass, solution and material. R_t represents the carrier transmission resistance inside the photoanode, and R_{ct} represents the charge transfer resistance at the photoanode/electrolyte interface. As expected, an obvious decrease of R_s was observed as loading NiFe-LDHs/Ru onto BiVO_4 , and the R_{ct} s of three photoanodes follows the order of $3090 \Omega > 686.4 \Omega > 398.2 \Omega$ (Table S6). Such significant decrease of bulk and interfacial transfer resistance lead to an excellent charge transport performance of $\text{BiVO}_4/\text{NiFe-LDHs/Ru}$. Moreover, the Bode plots of as-prepared samples are also measured (Fig. S18), which showed the maximum space charge capacitance of $\text{BiVO}_4/\text{NiFe-LDHs/Ru}$.

Positive slope of Mott-Schottky (MS) curves reflect that these three samples are n-type semiconductors (Fig. 4i). Carrier concentration of photoanodes were calculated according to Eq. (6), indicating that the carrier concentration of $\text{BiVO}_4/\text{NiFe-LDHs/Ru}$ was significantly

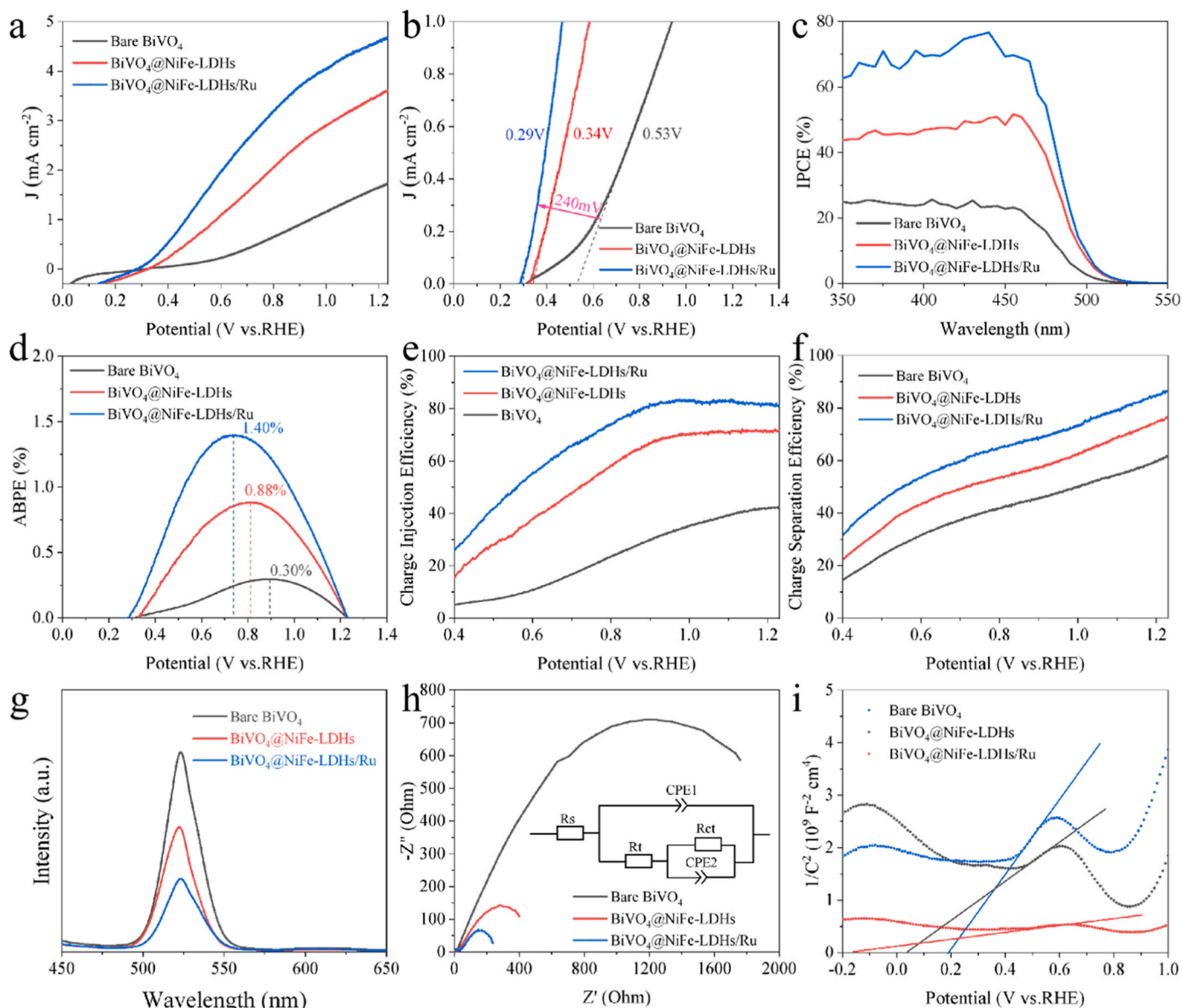


Fig. 4. (a) LSV curves, (b) onset potential, (c) IPCE curves, (d) ABPE curves, (e) η_{inj} , (f) η_{sep} , (g) PL spectra (excitation at 405 nm), (h) PEIS curves, and (i) Mott-Schottky plots of BiVO_4 , $\text{BiVO}_4@\text{NiFe-LDHs}$ and $\text{BiVO}_4@\text{NiFe-LDHs/Ru}$.

increased from $2.906 \times 10^{20} \text{ cm}^{-3}$ to $3.117 \times 10^{21} \text{ cm}^{-3}$ after loading of NiFe-LDHs/Ru on to BiVO_4 . The increased carrier concentration not only enhanced the conductivity in the bulk but also caused to a sharper band bending at the electrolyte interface, thus it can accelerate hole drift and suppress charge recombination in the depletion region [55]. In addition, Mott-Schottky measurements at different frequencies (Fig. S19) indicate that flat-band potentials of samples followed the order of BiVO_4 (0.188 V) > $\text{BiVO}_4@\text{NiFe-LDHs}$ (0.038 V) > $\text{BiVO}_4@\text{NiFe-LDHs/Ru}$ (−0.16 V). Decrease of flat-band potential and starting potential suggest a stronger driving force for H_2 evolution on cathode surface [56]. Open circuit photovoltage (OCP), which is caused by the splitting of the electron and hole quasi-Fermi level under illumination, can be calculated by $[\text{OCP} = \text{Open circuit photovoltage When Lighting (OCV}_{\text{light}}) - \text{Open circuit photovoltage in the Dark (OCV}_{\text{Dark}})]$, also verifying the existence of the strong intrinsic electric field [6]. The order of $\text{BiVO}_4@\text{NiFe-LDHs/Ru}$ (0.645 V) > $\text{BiVO}_4@\text{NiFe-LDHs}$ (0.529 V) > bare BiVO_4 (0.292 V) (Fig. S20) shows an obvious enhancement of intrinsic internal electric field by introduction of NiFe-LDHs/Ru, which also proves the highest concentration of holes on $\text{BiVO}_4@\text{NiFe-LDHs/Ru}$

on surface.

FT-IR spectra of BiVO_4 , $\text{BiVO}_4@\text{NiFe-LDHs}$ and $\text{BiVO}_4@\text{NiFe-LDHs/Ru}$ indicated that loading of NiFe-LDHs on photoanode could increase surface hydrophilic groups (−OH) (Fig. S21). In addition, $\text{BiVO}_4@\text{NiFe-LDHs/Ru}$ showed an earlier start and faster increase in current density compared to other samples in the dark LSV curve (Fig. 5a), exhibiting the highest electrocatalytic activity. The electrochemical double layer capacitances (Cdl), which is related to the electrochemical active surface area (ECSA) of the electrode, are estimated via cyclic voltammetry (CV) curves under various scan rates. Compared to BiVO_4 (0.143 mF cm^{-2}) and $\text{BiVO}_4@\text{NiFe-LDHs}$ (0.181 mF cm^{-2}), $\text{BiVO}_4@\text{NiFe-LDHs/Ru}$ possesses higher Cdl (0.248 mF cm^{-2}) (Fig. 5c–f), which suggests anchoring of Ru can provide more active sites for OER. About 115.7 mmol of oxygen and 231.5 mmol of hydrogen are generated in total after 3 h (Fig. 5b). Most of photogenerated electrons and holes of $\text{BiVO}_4@\text{NiFe-LDHs/Ru}$ participated in decomposing water into H_2 and O_2 , achieving the highest total Faraday efficiency of 91 %.

Previous work demonstrates that the photooxidation of Bi^{3+} by surface-accumulated holes was generally coupled with the dissolution of

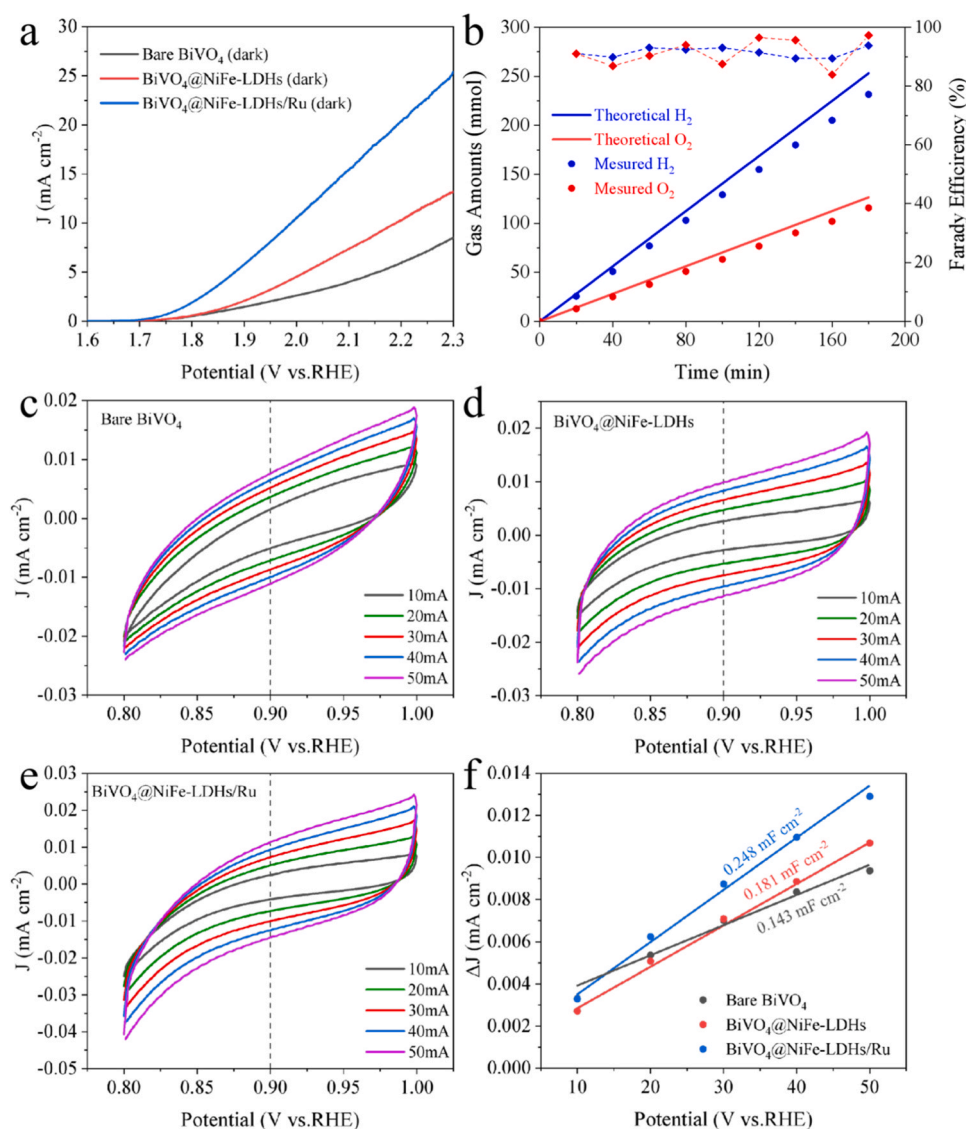


Fig. 5. (a) Dark polarization curves for water oxidation of BiVO_4 , $\text{BiVO}_4@\text{NiFe-LDHs}$ and $\text{BiVO}_4@\text{NiFe-LDHs/Ru}$. (b) H_2 and O_2 gases evolution curves at 1.23 V vs. RHE in KBi electrolyte under simulated AM 1.5 G illumination. (c-e) CV curves of bare BiVO_4 , $\text{BiVO}_4@\text{NiFe-LDHs}$ and $\text{BiVO}_4@\text{NiFe-LDHs/Ru}$ at different scanning rates, respectively. (f) Linear fitting of capacitance current and scanning rate.

V^{5+} , which destabilize the BiVO_4 lattice and increase the solubility of BiVO_4 [57]. As shown in Fig. 6a, $\text{BiVO}_4@\text{NiFe-LDHs/Ru}$ photoanode can maintain 94.8 % of initial photocurrent density at 1.23 V vs. RHE after 5 h without morphology changes, which exhibits superior stability than $\text{BiVO}_4@\text{NiFe-LDHs}$ (76.4 % for 1 h) and BiVO_4 (32.9 % for 1 h). In addition, the binding energies of Ru 3p in XPS kept stable (Fig. 6c), indicates Ru maintains a relatively low valence state. Furthermore, 10 mL of KBi electrolyte solution was sampled from the OER system for ICP-MS measurement (Fig. 6d), which indicates Ru anchored into photoanode can efficiently inhibit the V^{5+} and Fe/Ni dissolution. Especially for V^{5+} dissolution, it was decreased from 173.1 $\mu\text{g/L}$ to 4.1 $\mu\text{g/L}$ after Ru SAs anchored, which can be attributed to the lattice stabilization due to the Ru-O-M bond formation. Besides, Cs-corrected STEM image (Fig. S2c,d) of $\text{BiVO}_4@\text{NiFe-LDHs/Ru}$ after stability test also shows that Ru SAs are uniform dispersed on photoanode, without obvious dissolution or clustering.

3.3. Density functional theory (DFT) calculation

To theoretically analyze the significant improvement of OER

performance of $\text{BiVO}_4@\text{NiFe-LDHs/Ru}$, DFT calculation was performed based on the system with four-electron reaction pathways. The negative adsorption energy shows that the growth mechanism of LDHs on the surface of BiVO_4 is the preferential growth of the Ni-OH motif (Table S8). Previous work demonstrates Fe is the main active site in NiFe-LDHs [50,58], thus both Fe and Ru are considered as the main active sites with M-O single bond (M = Fe and Ru) during the DFT calculation. Gibbs free energy diagram (FED) indicates that the third step ($\text{*O} + \text{OH}^- \rightarrow \text{*OOH} + \text{e}^-$) is a rate-determined step (RDS) for OER in alkaline condition. $\Delta\text{G}_{\text{III}}$ values of Ru (2.39 eV) in $\text{BiVO}_4@\text{NiFe-LDHs/Ru}$ is lower than that of Fe (2.54 eV) (Fig. 7), which confirms the main active site of Ru for OER and indicates that isolated Ru SAs have significantly contributed toward accelerating the OER kinetics.

4. Conclusion

In the present work, novel $\text{BiVO}_4@\text{NiFe-LDHs/Ru}$ photoanode was fabricated for enhancement of OER in photoelectrochemical water splitting. Ru atoms anchored to NiFe-LDHs to form Ru-O-M bonds via oxygen coordination not only induced the spatial electron

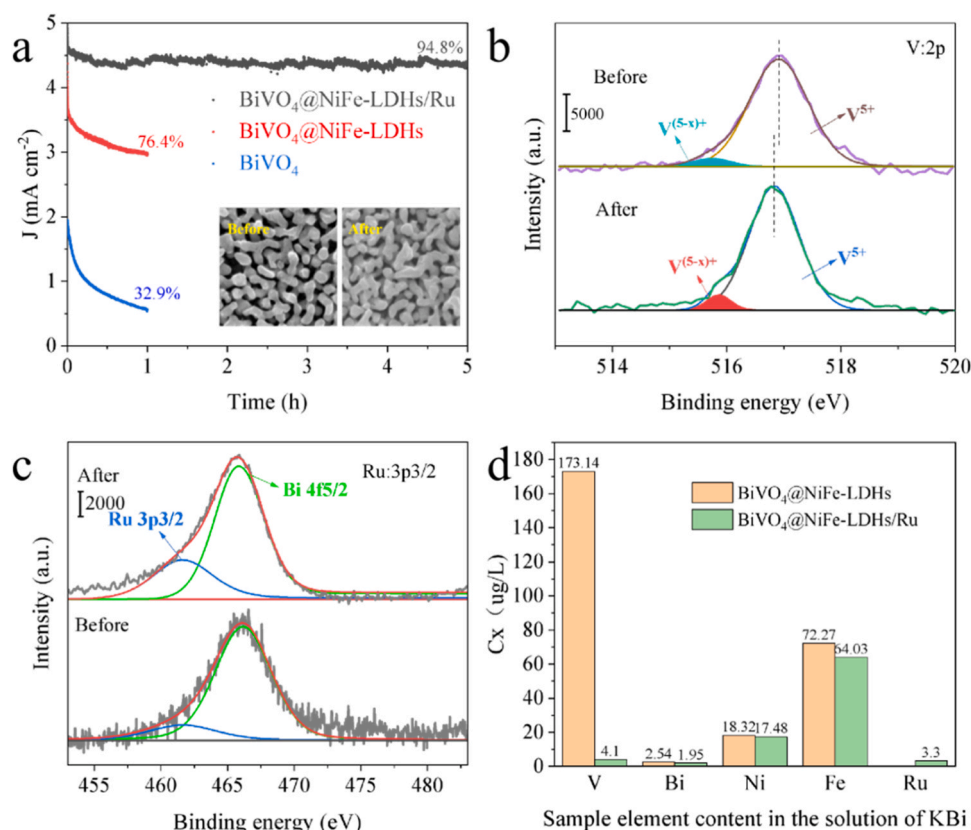


Fig. 6. (a) Photocurrent density stability of bare BiVO_4 , $\text{BiVO}_4/\text{NiFe-LDHs}$ and $\text{BiVO}_4/\text{NiFe-LDHs}/\text{Ru}$ photoanodes at 1.23 V vs. RHE for 5 h. XPS spectra of (b) V 2p and (c) Ru 3p of the $\text{BiVO}_4/\text{NiFe-LDHs}/\text{Ru}$ photoanode before and after stability measurement. (d) Element content in the solution of KBi after stability test.

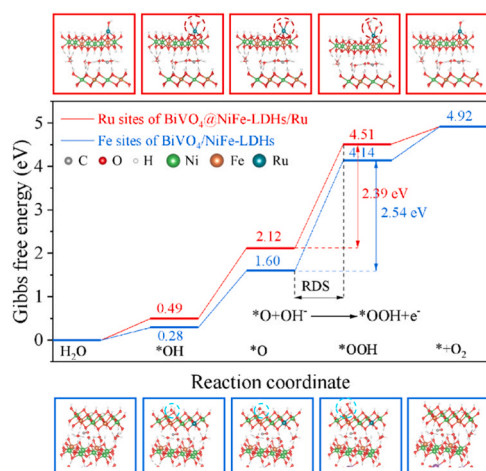


Fig. 7. Free energy diagram for OER pathway on $\text{BiVO}_4/\text{NiFe-LDHs}$ and $\text{BiVO}_4/\text{NiFe-LDHs}/\text{Ru}$ based on four-electron pathway, and reaction steps of Ru and Fe elements as active sites are shown in the illustration.

rearrangement for charge carriers transfer and separation, but also decrease the reaction energy barrier of rate-determining step. Combining with the synergistic effect of Ru and NiFe-LDHs, $\text{BiVO}_4/\text{NiFe-LDHs}/\text{Ru}$ achieves the high photocurrent density of $4.65 \text{ mA}/\text{cm}^2$ at 1.23 V vs. RHE at AM 1.5 G, and it remained 94.8 % of the value of initial photocurrent density within 5 h. This work provided new ideas to decrease reaction energy barrier of rate-determining step of OER, also expanding the application of Ru SAs in PEC water splitting.

CRediT authorship contribution statement

Yunshuyu Sun (First author): Writing- Original draft preparation, Conceptualization, Methodology, Investigation. **Hao Li:** Investigation, Methodology, Data curation. **Yao Hu:** Visualization, Conceptualization. **Jinnan Wang (Corresponding author):** Conceptualization, Supervision, Project administration, Writing - Review & Editing. **Aimin Li:** Validation, Data curation. **Philippe François-Xavier Corvini:** Visualization, Writing- Reviewing and Editing.

Declaration of Competing Interest

The authors declare that they have no known competing financial interests or personal relationships that could have appeared to influence the work reported in this paper.

Data availability

No data was used for the research described in the article.

Acknowledgements

This research was supported by National Natural Science Foundation of China (No. 52070095), Water Conservancy Technology Project of Jiangsu province (2022037) and Social development project of Jiangsu province (BE2022771).

Appendix A. Supporting information

Supplementary data associated with this article can be found in the online version at [doi:10.1016/j.apcatb.2023.123269](https://doi.org/10.1016/j.apcatb.2023.123269).

References

- [1] A. Fujishima, K. Honda, Electrochemical photolysis of water at a semiconductor electrode, *Nature* 238 (1972), 37–.
- [2] P. Lianos, Review of recent trends in photoelectrocatalytic conversion of solar energy to electricity and hydrogen, *Appl. Catal. B: Environ.* 210 (2017) 235–254.
- [3] X. Sheng, T. Xu, X. Feng, Rational design of photoelectrodes with rapid charge transport for photoelectrochemical applications, *Adv. Mater.* 31 (2019), e1805132.
- [4] F. Wang, Q. Ding, J. Ding, Y. Bai, H. Bai, W. Fan, Frustrated Lewis pairs boosting photoelectrochemical nitrate reduction over ZnIn₂S₄/BiVO₄ heterostructure, *Chem. Eng. J.* 450 (2022).
- [5] H. Bai, F. Wang, Q. Ding, W. Xie, H. Li, G. Zheng, W. Fan, Construction of frustrated Lewis pair sites in CeO₂(2-C)/BiVO₄(4) for photoelectrochemical nitrate reduction, *Inorg. Chem.* 62 (2023) 2394–2403.
- [6] J.H. Kim, J.S. Lee, Elaborately modified BiVO₄(4) photoanodes for solar water splitting, *Adv. Mater.* 31 (2019), e1806938.
- [7] D.K. Lee, D. Lee, M.A. Lumley, K.S. Choi, Progress on ternary oxide-based photoanodes for use in photoelectrochemical cells for solar water splitting, *Chem. Soc. Rev.* 48 (2019) 2126–2157.
- [8] W. Bai, Y. Zhou, G. Peng, J. Wang, A. Li, P.F.-X. Corvini, Engineering efficient hole transport layer Ferrihydrite-MXene on BiVO₄ photoanodes for photoelectrochemical water splitting: work function and conductivity regulated, *Appl. Catal. B: Environ.* 315 (2022).
- [9] I. Grigioni, K.G. Stamplecoskie, D. Jara, M.V. Dozzi, A. Oriana, G. Cerullo, P. V. Kamat, E. Selli, The wavelength dependent ultrafast charge carrier separation in the WO₃/BiVO₄ coupled system, *ACS Energy Lett.* 6 (2017) 1362–1367.
- [10] T.W. Kim, Y. Ping, G.A. Galli, K.S. Choi, Simultaneous enhancements in photon absorption and charge transport of bismuth vanadate photoanodes for solar water splitting, *Nat. Commun.* 6 (2015) 8769.
- [11] X. Pang, H. Bai, H. Zhao, W. Fan, W. Shi, Efficient electrocatalytic oxidation of 5-hydroxymethylfurfural coupled with 4-nitrophenol hydrogenation in a water system, *ACS Catal.* 12 (2022) 1545–1557.
- [12] X. Pang, H. Bai, Y. Huang, H. Zhao, G. Zheng, W. Fan, Mechanistic insights for dual-species evolution toward 5-hydroxymethylfurfural oxidation, *J. Catal.* 417 (2023) 22–34.
- [13] J.-M. Wu, Y. Chen, L. Pan, P. Wang, Y. Cui, D. Kong, L. Wang, X. Zhang, J.-J. Zou, Multi-layer monoclinic BiVO₄ with oxygen vacancies and V⁴⁺ species for highly efficient visible-light photoelectrochemical applications, *Appl. Catal. B: Environ.* 221 (2018) 187–195.
- [14] S. Wang, T. He, P. Chen, A. Du, K.K. Ostrikov, W. Huang, L. Wang, In situ formation of oxygen vacancies achieving near-complete charge separation in planar BiVO₄(4) photoanodes, *Adv. Mater.* 32 (2020), e2001385.
- [15] P. Lettenmeier, L. Wang, U. Golla-Schindler, P. Gazdzicki, N.A. Canas, M. Handl, R. Hiesgen, S.S. Hosseiny, A.S. Gago, K.A. Friedrich, Nanosized IrO(x)-Ir catalyst with relevant activity for anodes of proton exchange membrane electrolysis produced by a cost-effective procedure, *Angew. Chem. Int. Ed. Engl.* 55 (2016) 742–746.
- [16] T. Reier, H.N. Nong, D. Teschner, R. Schlögl, P. Strasser, Electrocatalytic oxygen evolution reaction in acidic environments - reaction mechanisms and catalysts, *Adv. Energy Mater.* 7 (2017).
- [17] B.Y. Xia, Y. Yan, N. Li, H.B. Wu, X.W. Lou, X. Wang, A metal-organic framework-derived bifunctional oxygen electrocatalyst, *Nat. Energy* 1 (2016).
- [18] C. Janáky, W. Chanmanee, K. Rajeshwar, On the substantially improved photoelectrochemical properties of nanoporous WO₃ through surface decoration with RuO₂, *Electrocatalysis* 4 (2013) 382–389.
- [19] P. Dias, L. Andrade, A. Mendes, Hematite-based photoelectrode for solar water splitting with very high photovoltage, *Nano Energy* 38 (2017) 218–231.
- [20] N. Danilovic, R. Subbaraman, K.C. Chang, S.H. Chang, Y.J. Kang, J. Snyder, A. P. Paulikas, D. Strmcnik, Y.T. Kim, D. Myers, V.R. Stamenkovic, N.M. Markovic, Activity-stability trends for the oxygen evolution reaction on monometallic oxides in acidic environments, *J. Phys. Chem. Lett.* 5 (2014) 2474–2478.
- [21] S. Cherevko, S. Geiger, O. Kasian, N. Kulyk, J.-P. Grote, A. Savaş, B.R. Shrestha, S. Merzlikin, B. Breitbach, A. Ludwig, K.J.J. Mayrhofer, Oxygen and hydrogen evolution reactions on Ru, RuO₂, Ir, and IrO₂ thin film electrodes in acidic and alkaline electrolytes: a comparative study on activity and stability, *Catal. Today* 262 (2016) 170–180.
- [22] I. Roger, M.A. Shipman, M.D. Symes, Earth-abundant catalysts for electrochemical and photoelectrochemical water splitting, *Nat. Rev. Chem.* 1 (2017).
- [23] X. Zhang, P. Zhai, Y. Zhang, Y. Wu, C. Wang, L. Ran, J. Gao, Z. Li, B. Zhang, Z. Fan, L. Sun, J. Hou, Engineering single-atomic Ni-N(4)-O sites on semiconductor photoanodes for high-performance photoelectrochemical water splitting, *J. Am. Chem. Soc.* 143 (2021) 20657–20669.
- [24] P. Li, M. Wang, X. Duan, L. Zheng, X. Cheng, Y. Zhang, Y. Kuang, Y. Li, Q. Ma, Z. Feng, W. Liu, X. Sun, Boosting oxygen evolution of single-atomic ruthenium through electronic coupling with cobalt-iron layered double hydroxides, *Nat. Commun.* 10 (2019) 1711.
- [25] D. Zhao, Z. Zhuang, X. Cao, C. Zhang, Q. Peng, C. Chen, Y. Li, Atomic site electrocatalysts for water splitting, oxygen reduction and selective oxidation, *Chem. Soc. Rev.* 49 (2020) 2215–2264.
- [26] Y. Miao, J. Liu, L. Chen, H. Sun, R. Zhang, J. Guo, M. Shao, Single-atomic-Co cocatalyst on (040) facet of BiVO₄ toward efficient photoelectrochemical water splitting, *Chem. Eng. J.* 427 (2022).
- [27] M.D. Marcinkowski, M.T. Darby, J. Liu, J.M. Wimbles, F.R. Lucci, S. Lee, A. Michaelides, M. Flytzani-Stephanopoulos, M. Stamatakis, E.C.H. Sykes, Pt/Cu single-atom alloys as coke-resistant catalysts for efficient C-H activation, *Nat. Chem.* 10 (2018) 325–332.
- [28] K. Song, H. Hou, D. Zhang, F. He, W. Yang, In-situ cation-exchange strategy for engineering single-atomic Co on TiO₂ photoanode toward efficient and durable solar water splitting, *Appl. Catal. B: Environ.* 330 (2023).
- [29] P. Xia, C. Wang, Q. He, Z. Ye, I. Sirés, MOF-derived single-atom catalysts: The next frontier in advanced oxidation for water treatment, *Chem. Eng. J.* 452 (2023).
- [30] J. Zhao, Z. Chen, Single Mo atom supported on defective boron nitride monolayer as an efficient electrocatalyst for nitrogen fixation: a computational study, *J. Am. Chem. Soc.* 139 (2017) 12480–12487.
- [31] Y. Li, Q. Wang, X. Hu, Y. Meng, H. She, L. Wang, J. Huang, G. Zhu, Constructing NiFe-metal-organic frameworks from NiFe-layered double hydroxide as a highly efficient cocatalyst for BiVO₄ photoanode PEC water splitting, *Chem. Eng. J.* 433 (2022).
- [32] D. Zhou, P. Li, X. Lin, A. McKinley, Y. Kuang, W. Liu, W.F. Lin, X. Sun, X. Duan, Layered double hydroxide-based electrocatalysts for the oxygen evolution reaction: identification and tailoring of active sites, and superaerophobic nanoarray electrode assembly, *Chem. Soc. Rev.* 50 (2021) 8790–8817.
- [33] Q. Wang, T. Niu, L. Wang, J. Huang, H. She, NiFe layered double-hydroxide nanoparticles for efficiently enhancing performance of BiVO₄ photoanode in photoelectrochemical water splitting, *Chin. J. Catal.* 39 (2018) 613–618.
- [34] J. Guo, X. Yang, S. Bai, X. Xiang, R. Luo, J. He, A. Chen, Effect of Mo doping and NiFe-LDH cocatalyst on PEC water oxidation efficiency, *J. Colloid Interface Sci.* 540 (2019) 9–19.
- [35] D. Friebe, M.W. Louie, M. Bajdich, K.E. Sanwald, Y. Cai, A.M. Wise, M.J. Cheng, D. Sokaras, T.C. Weng, R. Alonso-Mori, R.C. Davis, J.R. Bargar, J.K. Norskov, A. Nilsson, A.T. Bell, Identification of highly active Fe sites in (Ni,Fe)OOH for electrocatalytic water splitting, *J. Am. Chem. Soc.* 137 (2015) 1305–1313.
- [36] J.M. Barforoush, T.E. Seufferling, D.T. Jantz, K.R. Song, K.C. Leonard, Insights into the active electrocatalytic areas of layered double hydroxide and amorphous nickel-iron oxide oxygen evolution electrocatalysts, *ACS Appl. Energy Mater.* 1 (2018) 1415–1423.
- [37] C. Wang, M. Humayun, D.P. Debecker, Y. Wu, Electrocatalytic water oxidation with layered double hydroxides confining single atoms, *Coord. Chem. Rev.* 478 (2023).
- [38] Q.Q. Chen, C.C. Hou, C.J. Wang, X. Yang, R. Shi, Y. Chen, Ir(4+)-doped NiFe LDH to expedite hydrogen evolution kinetics as a Pt-like electrocatalyst for water splitting, *Chem. Commun. (Camb.)* 54 (2018) 6400–6403.
- [39] G. Chen, T. Wang, J. Zhang, P. Liu, H. Sun, X. Zhuang, M. Chen, X. Feng, Accelerated hydrogen evolution kinetics on NiFe-layered double hydroxide electrocatalysts by tailoring water dissociation active sites, *Adv. Mater.* 30 (2018).
- [40] T.W. Kim, K.-S. Choi, Nanoporous BiVO₄ photoanodes with dual-layer oxygen evolution catalysts for solar water splitting, *Science* 343 (2014) 990–994.
- [41] G. Kresse, J. Furthmüller, Efficiency of ab-initio total energy calculations for metals and semiconductors using a plane-wave basis set, *Comput. Mater. Sci.* 6 (1996) 15–50.
- [42] G. Kresse, J. Furthmüller, Efficient iterative schemes for ab initio total-energy calculations using a plane-wave basis set, *Phys. Rev. B* 54 (1996) 11169–11186.
- [43] J.P. Perdew, K. Burke, M. Ernzerhof, Generalized gradient approximation made simple, *Phys. Rev. Lett.* 78 (1996) 3865–3868.
- [44] Y. Zhang, Y. Li, D. Ni, Z. Chen, X. Wang, Y. Bu, J.P. Ao, Improvement of BiVO₄ photoanode performance during water photo-oxidation using Rh-doped SrTiO₃ perovskite as a co-catalyst, *Adv. Funct. Mater.* 29 (2019).
- [45] M. Wang, Z. Wang, B. Zhang, W. Jiang, X. Bao, H. Cheng, Z. Zheng, P. Wang, Y. Liu, M.-H. Whangbo, Y. Li, Y. Dai, B. Huang, Enhancing the photoelectrochemical water oxidation reaction of BiVO₄ photoanode by employing carbon spheres as electron reservoirs, *ACS Catal.* 10 (2020) 13031–13039.
- [46] P. Li, X. Chen, H. He, X. Zhou, Y. Zhou, Z. Zou, Polyhedral 30-faceted BiVO₄(4) microcrystals predominantly enclosed by high-index planes promoting photocatalytic water-splitting activity, *Adv. Mater.* 30 (2018).
- [47] J. Zhang, J. Liu, L. Xi, Y. Yu, N. Chen, S. Sun, W. Wang, K.M. Lange, B. Zhang, Single-atom Au/NiFe layered double hydroxide electrocatalyst: probing the origin of activity for oxygen evolution reaction, *J. Am. Chem. Soc.* 140 (2018) 3876–3879.
- [48] K. Mori, T. Taga, H. Yamashita, Isolated single-atomic Ru catalyst bound on a layered double hydroxide for hydrogenation of CO₂ to formic acid, *ACS Catal.* 7 (2017) 3147–3151.
- [49] P. Zhai, M. Xia, Y. Wu, G. Zhang, J. Gao, B. Zhang, S. Cao, Y. Zhang, Z. Li, Z. Fan, C. Wang, X. Zhang, J.T. Miller, L. Sun, J. Hou, Engineering single-atomic ruthenium catalytic sites on defective nickel-iron layered double hydroxide for overall water splitting, *Nat. Commun.* 12 (2021) 4587.
- [50] Y. Yang, Q.-N. Yang, Y.-B. Yang, P.-F. Guo, W.-X. Feng, Y. Jia, K. Wang, W.-T. Wang, Z.-H. He, Z.-T. Liu, Enhancing water oxidation of Ru single atoms via oxygen-coordination bonding with NiFe layered double hydroxide, *ACS Catal.* 13 (2023) 2771–2779.
- [51] B. Zhang, X. Huang, Y. Zhang, G. Lu, L. Chou, Y. Bi, Unveiling the activity and stability origin of BiVO₄ photoanodes with FeNi oxyhydroxides for oxygen evolution, *Angew. Chem. Int. Ed. Engl.* 59 (2020) 18990–18995.
- [52] S. Jin, X. Ma, J. Pan, C. Zhu, S.E. Sajj, J. Hu, X. Xu, L. Sun, Z. Yin, Oxygen vacancies activating surface reactivity to favor charge separation and transfer in nanoporous BiVO₄ photoanodes, *Appl. Catal. B: Environ.* 281 (2021).
- [53] L. Li, J. Li, J. Bai, Q. Zeng, L. Xia, Y. Zhang, S. Chen, Q. Xu, B. Zhou, Serial hole transfer layers for a BiVO₄ photoanode with enhanced photoelectrochemical water splitting, *Nanoscale* 10 (2018) 18378–18386.
- [54] Y. Liu, M. Xia, L. Yao, M. Mensi, D. Ren, M. Grätzel, K. Sivula, N. Guijarro, Spectroelectrochemical and chemical evidence of surface passivation at zinc ferrite (ZnFe₂O₄) photoanodes for solar water oxidation, *Adv. Funct. Mater.* 31 (2021).

- [55] M. Zhong, T. Hisatomi, Y. Kuang, J. Zhao, M. Liu, A. Iwase, Q. Jia, H. Nishiyama, T. Minegishi, M. Nakabayashi, N. Shibata, R. Niishiro, C. Katayama, H. Shibano, M. Katayama, A. Kudo, T. Yamada, K. Domen, Surface modification of CoO(x) loaded BiVO₄ photoanodes with ultrathin p-Type NiO layers for improved solar water oxidation, *J. Am. Chem. Soc.* 137 (2015) 5053–5060.
- [56] Y. Shi, Y. Yu, Y. Yu, Y. Huang, B. Zhao, B. Zhang, Boosting photoelectrochemical water oxidation activity and stability of Mo-doped BiVO₄ through the uniform assembly coating of NiFe–phenolic networks, *ACS Energy Lett.* 3 (2018) 1648–1654.
- [57] D.K. Lee, K.-S. Choi, Enhancing long-term photostability of BiVO₄ photoanodes for solar water splitting by tuning electrolyte composition, *Nat. Energy* 3 (2017) 53–60.
- [58] P.-F. Guo, Y. Yang, W.-J. Wang, B. Zhu, W.-T. Wang, Z.-Y. Wang, J.-L. Wang, K. Wang, Z.-H. He, Z.-T. Liu, Stable and active NiFeW layered double hydroxide for enhanced electrocatalytic oxygen evolution reaction, *Chem. Eng. J.* 426 (2021).